Fizika Nizkikh Temperatur, 2003, v. 29, No. 3, p. 303–320

Element-specific and site-specific ion desorption from adsorbed molecules by deep core-level photoexcitation at the *K*-edges

(Review Article)

Yuji Baba

Synchrotron Radiation Research Center, Japan Atomic Energy Research Institute
Tokai-mura, Naka-gun, Ibaraki-ken 319-1195, Japan
E-mail: ybaba@popsvr.tokai.jaeri.go.jp

Received November 20, 2002

This article reviews our recent works on the ion desorption from adsorbed and condensed molecules at low temperature following the core-level photoexcitations using synchrotron soft x-rays. The systems investigated here are adsorbed molecules with relatively heavy molecular weight containing third-row elements such as Si, P, S, and Cl. Compared with molecules composed of second-row elements, the highly element-specific and site-specific fragment-ion desorptions were observed when we tune the photon energy at the dipole-allowed $1s \rightarrow \sigma^*(3p^*)$ resonance. On the basis of the resonance Auger decay spectra around the 1*s* ionization thresholds, the observed highly specific ion desorption is interpreted by the localization of the excited electrons (here we call as «spectator electrons») in the antibonding σ^* orbital. In order to separate the direct photo-induced process from the indirect processes triggered by the secondary electrons, the photon-stimulated ion desorption was also investigated in well-controlled mono- and multilayered molecules. The results confirmed that the resonant photoexcitation not in the substrate but in the thin films of adsorbates plays a significant role in the realization of the highly specific ion desorption.

PACS: 79.20.La, 29.30.Kv

1. Introduction

Photo-induced processes at solid surfaces have attracted much attention not only as fundamental science but also as technological applications, because we can possibly synthesize new materials through non-thermal reactions. Among various photo-induced processes, those induced by energy-tunable synchrotron soft x-rays have been the focus of considerable attention because x-ray-induced reaction has the excellent potentials represented as «element-specificity» and «site-specificity». An x-ray-induced chemical reaction is triggered by the excitation and ionization of core-level electrons which are localized at the atomic site even in a multi-element material. Thus we can possibly excite a specific element or specific chemical-bond by tuning the energy of x-rays at the inner-shell ionization threshold of the specific element. Using this characteristic, there exists a possibility that we can control a chemical reaction at a solid surface. For example, we can cut a specific chemical bond around the specific element as if we were using «scissors or a knife». Recent progresses in this approach is reviewed in some of the articles Refs. 1–4.

One might want to know about «In what case we can cut a specific chemical bond?», or in other word, «Is there any general theory or general rule to realize a specific bond scission?». As to these questions, I would like to stress the following three general principles to realize the highly specific chemical bond scission by the core-level photoexcitation. Firstly, the photoexcitation at the *K*-edge is more efficient than those at the L_1-, $L_{2,3}$- and *M*-edges. This is simply understood by the absorption edge-jump, which is defined as the ratio of the photoionization cross sections σ_L/σ_H, where *L* and *H* refer, respectively, to the low- and high-energy sides of the absorption edges. The absorption edge-jumps of the *K*-edge in all of the elements are higher than those of the *L*- and *M*-edges in the respective elements [5]. Secondly, the element specificity clearly shows up with the increase in the difference in the atomic number of the two elements. This is simply estimated by the cal-

culated values of the photon-energy dependencies of the photoionization cross sections [6,7]. The typical example is observed for the deep core-level excitation of a heavy element in the light-element matrix. Similarly, the shallow core-level excitation of a light element in the heavy-element matrix is also effective. The third factor is the resonance effect. If the resonance excitation from the core to valence unoccupied orbitals in a compound is dipole-allowed transition, the absorption edge-jump dramatically increases, which may result in the highly specific fragmentation.

On the basis of the above speculations, this article mainly deals with the results for the ion desorption following the resonant photoexcitations at the *K*-edges for the adsorbed molecules. Especially, we concentrate on the ion desorption from relatively heavy molecules containing third-row elements such as Si, P, S, and Cl, because we found that the element specificity and site-specificity clearly show up in the $1s \rightarrow 3p^*(\sigma^*)$ resonant photoexcitation in the third-row elements. Nest I shall discuss the mechanism of the observed highly specific ion desorption from condensed molecules on the basis of the photon-energy dependencies of the desorption yields and the Auger decay spectra. In the adsorbed systems, the chemical reaction by the core-level excitation is caused by two processes, i.e., direct process triggered by the core-level photoexcitation and indirect processes which are induced by the secondary electrons. Therefore I present finally the results for the stimulated ion desorption from well-controlled mono- and multilayers in order to elucidate the mechanism more clearly by separating these two processes.

2. General descriptions for element-specific and site-specific bond scissions

The specific fragmentation and desorption initiated by core-level photoexcitation is characterized by the different patterns shown in Fig. 1. The first is the «element-specific» reaction depicted in Fig. 1(1). This is the most principal characteristics of core-level photoexcitation. In this simplified model, the photon energy is tuned at the core-level of the element C. The element C is selectively excited leading to the breaking of only the B—C bond but not the A—B bond. For solid surfaces, the desorption of the element C is expected. The second case is the «site-specific» reaction. This is further divided into two cases. In the upper model (*a*), the core-levels of the elements B have two energy levels (B_1 and B_2) depending on the chemical environment. This energy shift is called as a chemical shift. If we tune the energy of x-ray at the core-level of B_2, only B_2 atom is excited without exciting B_1 atom. Consequently, B_2—C or B_2—B_1 bond would be broken without cutting the A—B_1 bond. In the lower model (*b*), the element B has only single core-level state, but the valence unoccupied state is divided into two levels localized at the B—C and A—B bond. In this figure, the core electrons in the element B are resonantly excited into the unoccupied state which is localized at the B—C bond. If this state has an antibonding character, the B—C bond would be broken but not A—B bond.

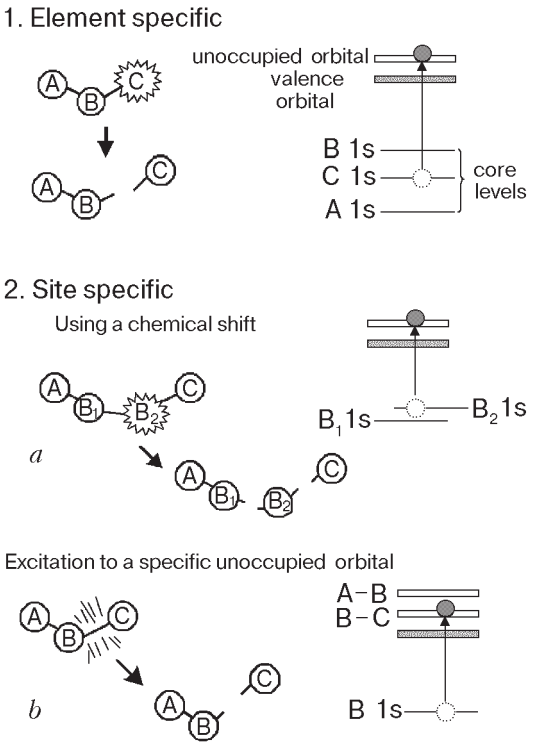

Fig. 1. Schematics of specific chemical reaction induced by inner-shell electron excitation using energy-tunable synchrotron soft x-rays. The photon energies are tuned at the resonance excitation from core-levels to the valence unoccupied orbitals.

3. Experimental details

The schematic diagram around the sample is shown in Fig. 2. The samples investigated here are molecules containing third-row elements such as silane derivatives, disulfide and chloromethane. Most of the samples are liquid at room temperature. The samples were purified and degassed through several freeze-pump-thaw cycles in the gas dosing vacuum system connected with the analyzer chamber. Then the samples are dosed onto the clean surface of a metal or semiconductor single crystal cooled at 80 K.

Most of the experiments were conducted at the beam line (BL, 27A) station of the Photon Factory in the High Energy Accelerator Research Organization (KEK-PF).

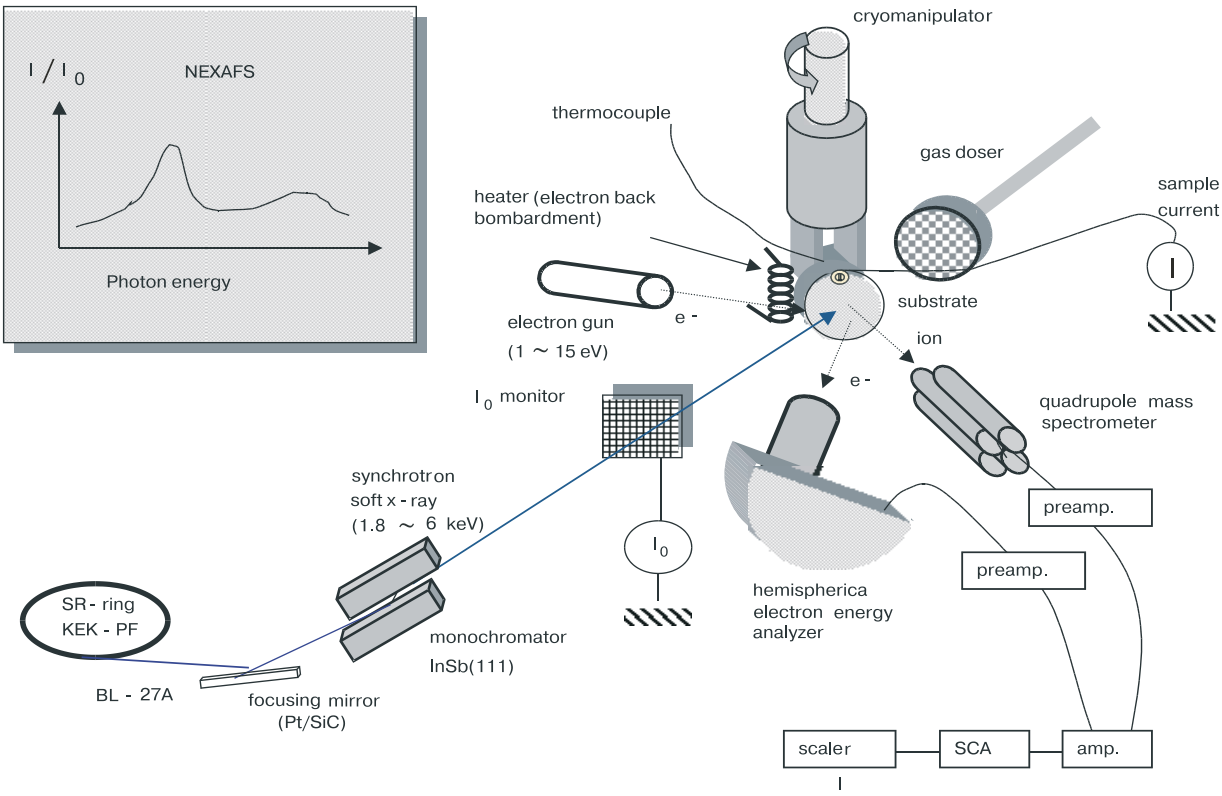

Fig. 2. Schematic diagram of the apparatus used for the experiments in this review.

The detailed performance of this beam line was described elsewhere [8]. The energy range of this beam line is 1.8–6 keV, which covers the *K*-edges of third-row elements such as silicon, phosphorus, sulfur, and chlorine. For comparison, the resonance experiments at the *K*-edges for second-row elements such as carbon and oxygen were also carried out at the beam line (BL, 7A) station of the KEK-PF.

The ultrahigh vacuum system used in this work consisted of a cryomanipulator which can rotate around the vertical axis, electron back bombardment system for sample heating, temperature control system, quadrupole mass spectrometer (Q-mass), hemispherical electron energy analyzer, low-energy electron diffraction (LEED), sputter ion gun, low-energy electron gun, and gas doser. The x-ray absorption spectra were taken by plotting the sample drain current as a function of the photon energy. This method is called as «total electron yield» mode. The x-ray absorption spectrum around the core-level threshold is termed as «x-ray absorption near-edge structure» (XANES) or «near edge x-ray absorption fine structure» (NEXAFS). The desorbed ions were detected by the Q-mass operating in a pulse counting mode. The photon flux was always normalized by the drain current of the copper mesh located in front of the sample.

4. Element-specific desorption from condensed molecules

4.1. Condensed $SiCl_4$

The most essential question concerning the x-ray-induced processes in solid is: «Are there any differences, when the core-levels in the different elements are excited in multi-element solid?». However, the clear answer for this simple question has not yet been given. For the photon-stimulated desorption from condensed light molecules, the fragment-ion desorption from solid CO and NO following the *K*-edge excitations have been investigated by Rosenberg et al. [9]. For solid CO, they have observed the enhancement of the C^+/O^+ ratios at about 30 % at the C *K*-edge photoexcitation. It is obvious that the element-specificity of the desorption primarily depends on the ratio of the photoionization cross sections, $\sigma_i/\sigma_{\text{total}}$, where σ_i and σ_{total} are the inner-shell photoionization cross sections of the element i and the total molecule, respectively. Based on this simple speculation, it can be deduced that the element-specificity more clearly shows up in heavy element rather than light element.

The typical example for heavy molecule containing third-row elements is shown in Fig. 3 [10]. This figure compares the mass spectral patterns of the desorbed ions from condensed $SiCl_4$ molecules irradiated by

two kinds of photon energies corresponding to the Si *K*-edge (upper spectrum) and the Cl *K*-edge (lower spectrum). The photon-energy dependencies of the ionization cross sections of silicon and chlorine are shown at the top of the figure. The x-ray absorption near-edge structure spectrum is displayed in the small inset in each mass spectrum. The photon energies are tuned at the respective resonance maxima of the

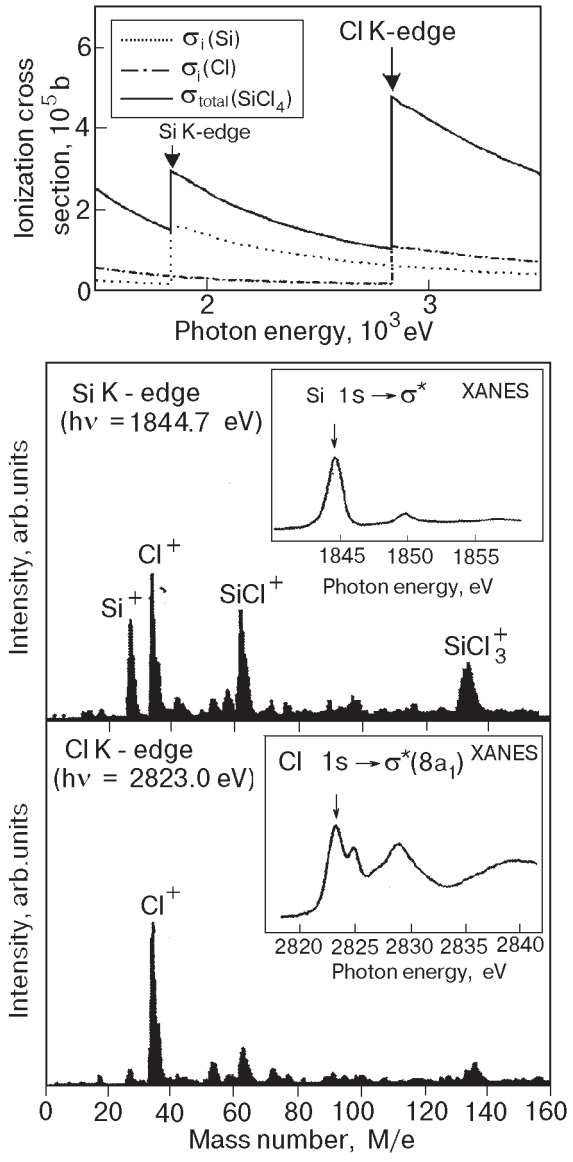

Fig. 3. Comparison of the mass spectral patterns of the desorbed ions from condensed $SiCl_4$ molecules irradiated by two kinds of photon energies corresponding to the Si and Cl *K*-edges. The x-ray absorption near-edge structure taken by the total electron yield is displayed in the small inset in each mass spectrum. The photon energy for the mass spectral measurements was tuned at the respective resonance maximum of $1s \rightarrow \sigma^*$ indicated in the XANES spectra. The photon-energy dependencies of the ionization cross sections of silicon and chlorine [6] are shown at the top of the figure.

$1s \rightarrow \sigma^*(3p^*)$ excitations. For Si *K*-edge excitation, not only molecular ions ($SiCl^+$, $SiCl_3^+$) but also atomic ions (Si^+, Cl^+) are desorbed in comparable intensity, while most of the desorbed species following the Cl *K*-edge excitation are atomic Cl^+ ions. This is quite surprising because the core-level excitation is primarily followed by the Auger decay whose time scale is in the order of 10^{-15} s, which is faster by about three orders of magnitudes than the time scale of the chemical bond breaking. If the delocalization of the excitation happens before the chemical bond scission, the Auger electrons and the succeeding secondary electrons are the main trigger of the bond breaking and ion desorption. This means that the same mass patterns should be observed even if the different core-levels are excited. The present results suggest that the time scale of the Si—Cl bond scission and Cl^+ desorption is comparable to or faster than that of the delocalization of the excited states. Such highly element-specific desorption has been also observed for simple condensed molecules composed of two kinds of third-row elements, such as PCl_3, S_2Cl_2 [11,12].

4.2. Condensed silicon alkoxides

For the future application, the element-specificity of core-level excitation has a potential in the photochemical processes at semiconductor surfaces. In silicon technology, for example, one of the key techniques is the deposition and etching of semiconductor surfaces without heating and damaging the substrate. The photochemical process is one of the candidate methods for this purpose. For metal-oxide-semiconductor (MOS) devices, it is required to fabricate an ultrathin and homogeneous oxide overlayer in a controlled small area on the semiconductor substrate. Silicon alkoxides such as tetramethoxysilane (TMOS) and tetraethoxysilane (TEOS) are excellent source materials for SiO_2 deposition on Si surface because of the conformal step coverage of SiO_2 layer and its nontoxic property. Niwano et al. have demonstrated the potentiality of synchrotron-radiation-induced CVD for the fabrication of SiO_2 films on Si using silicon alkoxides as source materials [13–15]. In their works, broad-band synchrotron radiation in the vacuum ultraviolet (VUV) region emerging from the bending magnet has been used, therefore the photon-energy dependencies of the reaction remain unclear.

Our results using monochromatized synchrotron beam are shown in Fig. 4 [16]. The left figures show the mass spectra of desorbed ions from condensed $Si(OCH_3)_4$ following (*a*) silicon *K*-edge, (*b*) carbon *K*-edge, and (*c*) oxygen *K*-edge excitations. The thickness of the adsorbates was 300 layers. The photon energy of each spectrum was tuned just at the $1s \rightarrow \sigma^*$ reso-

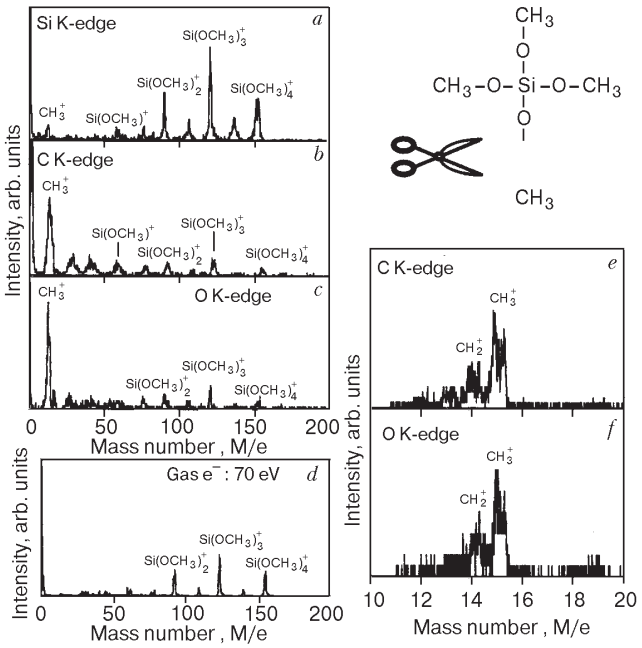

Fig. 4. Mass spectra for desorbed ions from condensed $Si(OCH_3)_4$ following silicon *K*-edge (*a*), carbon *K*-edge (*b*), and oxygen *K*-edge photoexcitations (*c*). The photon energy of each spectrum is tuned just at the $1s \rightarrow \sigma^*$ resonance maximum of the respective absorption edge. The mass spectrum of fragment ions for gas-phase $Si(OCH_3)_4$ excited by 70-eV electrons (so called cracking pattern) represents column (*d*). Mass spectra in narrow regions with higher mass-resolution for C *K*-edge (*e*) and O *K*-edge excitations are shown in right hand (*f*).

nance maximum of the respective absorption edges. For comparison, the mass spectrum of fragment ions for gas-phase $Si(OCH_3)_4$ excited by 70-eV electrons (so called cracking pattern) is displayed in the Fig. 4,*d*. Since the electron energy for the gas-phase spectrum is lower than the Si 2*p*, C 1*s* and, O 1*s* thresholds, the gas-phase spectrum exhibits an ionic fragmentation pattern following not inner-shell excitation but valence excitation. The desorption spectrum at the Si *K*-edge excitation resembles the gas-phase one. For the C and O *K*-edge excitations, on the other hand, the most intense peak (except for H^+) is located around $M/e = 15$. The long-time measurements with higher mass-resolution shown in the Fig. 4,*e*,*f* reveal that the most intense peaks originate from the CH_3^+ ions ($M/e = 15$), but no O^+ ions ($M/e = 16$) are observed. This indicates that the C—O bonds are selectively cut off following both carbon and oxygen *K*-edge excitations, but the Si—O bonds mostly remain unbroken. These results shed light on the possibility of selective C—O bond scission in condensed $Si(OCH_3)_4$ using monochromitized synchrotron radiation.

5. Site-specific desorption

5.1. General descriptions

Next I shall show the examples of the site-specific desorption shown in Fig. 1(2). If the molecule has the same elements but inequivalent chemical environments, we can selectively excite each atom shown in Fig. 1(2,*a*). Such example was firstly found for gas-phase molecule by Eberhardt et al. [17]. They selectively excite two kinds of carbon atoms in acetone, which has inequivalent carbon atoms, and succeeded in observing the different ionic photofragmentation patterns depending on the atomic site being excited. Although some of the controversy still remains as to their results, this pioneering work stimulated the site-specific fragmentation in molecules following inner-shell photoexcitation. The clear examples for the site-specific fragmentation using chemical shifts were recently reported by Nagaoka et al. for condensed molecules [18,19]. Even for the equivalent molecule like N_2, Romberg et al. recently demonstrated that one of the two nitrogen atoms in adsorbed N_2 molecule can be selectively excited using high resolution synchrotron beam [20,21]. They observed different desorption patterns depending on the atomic site being excited.

In the followings, I shall concentrate on the second case in Fig. 1(2,*b*) The site-specific ion desorption from solid surface represented by Fig. 1(2,*b*) has been reported in many systems, such as organic polymers [22–27], and adsorbed molecules [28–40] following the *K*-edge excitation in second-row elements. Here I shall show the examples of the highly site-specific ion desorption from adsorbed molecules following the $1s \rightarrow 3p^*$ resonance in the third-row elements, because the site-specificity clearly show up in deep-core excitations as described previously.

5.2. Adsorbed $Si(CH_3)_3F$

Figure 5 shows the mass spectra of trimethyfuluorosilance ($Si(CH_3)_3F$, TMFS). The upper figure displays the mass pattern of desorbed ions from TMFS adsorbed on Cu (111) surface [39]. The thickness of the adsorbed layer is just one monolayer which was precisely calibrated. Due to high electronegative character of fluorine atom, the valence unoccupied orbitals of TMFS are split into two states. One is the σ^* orbitals localized at the Si—C bond (denoted as $\sigma^*_{(Si-C)}$), and the other is those localized at the Si—F bond (denoted as $\sigma^*_{(Si-F)}$). Here the photon energy was tuned at the resonance maximum from the Si 1*s* to unoccupied $\sigma^*_{(Si-F)}$ orbitals. For comparison, mass spectrum of fragment ions in gas-phase TMFS following the 70-eV electron impact is also shown in the lower figure. Electron impact produces many of

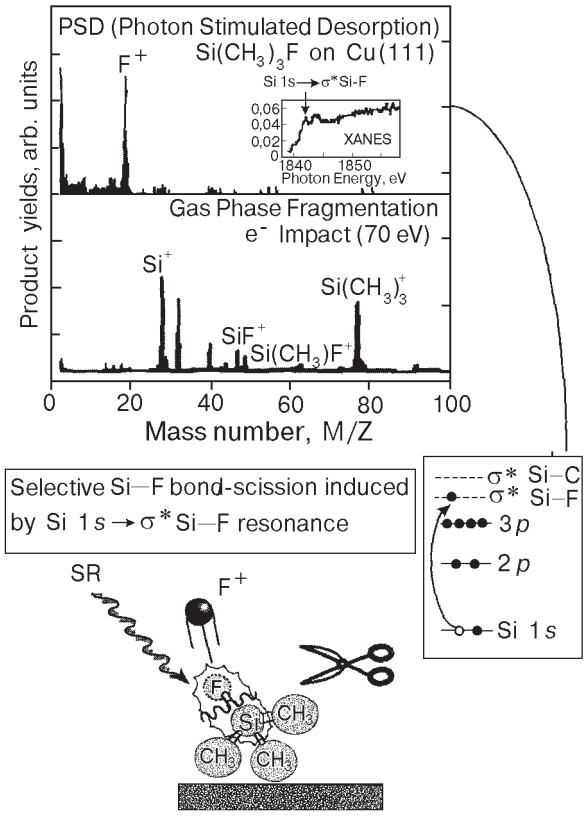

Fig. 5. Mass spectrum for desorbed ions from adsorbed $Si(CH_3)_3F$ following the Si 1*s* resonance photoexcitation (upper figure). Mass spectrum of fragment ions produced by 70 eV electron impact is shown in the lower figure.

fragment ions containing silicon, which exhibits the mass cracking pattern following the valence excitation. On the other hand, the Si $1s \rightarrow \sigma^*_{(Si-F)}$ resonance excitation in adsorbed TMFS results in the desorption of only F^+ ions other than hydrogen ions which are mostly abundant ions. The difference of two mass patterns clearly indicates that the resonant excitation from the Si 1*s* into the antibonding $\sigma^*_{(Si-F)}$ selectively break the Si—F bond without cutting the Si—C bond.

5.3. Condensed $(CH_3S)_2$

The data presented second is the fragment-ion desorption from condensed $(CH_3S)_2$ (dimethyldisulfide, DMDS) [30]. The sulfur atoms in this molecule are coordinated to two kinds of different atoms, i.e., sulfur and carbon. DMDS is chosen because this molecule is the simplest prototype of amino acid containing S—S bond such as cyctine, and the primary process of the x-ray-induced fragmentation is quite important in the fields of radiation biology.

XANES spectrum taken by the total electron yield mode for multilayered DMDS is displayed in Fig. 6,*a* as topmost spectrum (solid line). The sharp resonance peak with double structure (marked *A*) and broad one (marked *B*) are observed in this energy region. In comparison with many of the gas-phase XANES spectra for alkylated divalent sulfur compounds [41–43], the first intense peak *A* can be assigned as the S $1s \rightarrow \sigma^*$(S $3p^*$) excitation and the second broad peak *B* is ascribed to the shape resonance corresponding to the excitation into higher-energy unoccupied orbitals such as S $3d^*$ and S $5s^*$. It is noticeable that the peak *A* is further split into two components. Fig. 6,*b* is the same spectra but in an expanded energy scale. The energy separation of the two components in XANES spectrum is 1.2 eV. Such peak splitting in the S $1s \rightarrow \sigma^*$ is never seen in divalent sulfur compounds containing a single S atom, such as dimethyl sulfide [43]. The occupied valence shell of the ground state of DMDS is $(9a)^2(10a)^2(9b)^2(10b)^2(11b)^2(11a)^2(12a)^2(13a)^2(12b)^2$ [44]. The outermost 12*b* and 13*a* orbitals are almost nonbonding and their main components are S 3*p* orbitals [45]. The 12*a* orbital consists of σ(S—S) and 11*a* and 11*b* orbitals have σ(S—C) character [45]. The energy levels of the σ(S—S) and σ(S—C) orbitals for gas-phase DMDS have been measured by ultra-violet photoelectron spectroscopy (UPS) [46]. The energy separation between 11*a* and 12*a* orbitals in UPS spectrum is close to the present value of the energy splitting of the S $1s \rightarrow \sigma^*$ peak. It has been established that the relative energy levels of molecular orbitals scarcely change from gas phase to Van der Waals molecular condensate. This is indeed the case for the DMDS adsorbed on Cu (111) surface at various temperatures [46]. Considering a mirror-like structure between occupied and unoccupied levels in valence region, we assign the lower- and higher-energy components as the excitations from the S 1*s* to the σ* localized at the S—S bond (hereafter we refer to $\sigma^*_{(S-S)}$) and the σ* localized at the S—C bond (hereafter we refer to $\sigma^*_{(S-C)}$), respectively. This is consistent with the simple assignment of the XANES spectrum of gas-phase DMDS by Hitchcock et. al. [47]. Similar energy splittings in the S $1s \rightarrow \sigma^*$ resonance peaks were also observed in condensed layers of the S—S containing compounds such as dichlorodisulfide (Cl—S—S—Cl) and dibutyldisulfide (C_4H_9—S—S—C_4H_9) [48].

The desorbed species following the S *K*-edge excitation are mainly S^+ and CH_3^+ ions. The photon-energy dependencies of the S^+- and CH_3^+-ion yields are presented in Fig. 6,*a* as dotted curves. Also they are shown in Fig. 6,*b* in an expanded energy scale. Two different features are seen between electron-yield and desorption-yield curves. Firstly, the excitation at the shape resonance (peak *B* in the S^+ ions are desorbed mainly at the S $1s \rightarrow \sigma^*_{(S-S)}$ resonance while the CH_3^+ ions are desorbed predominantly at

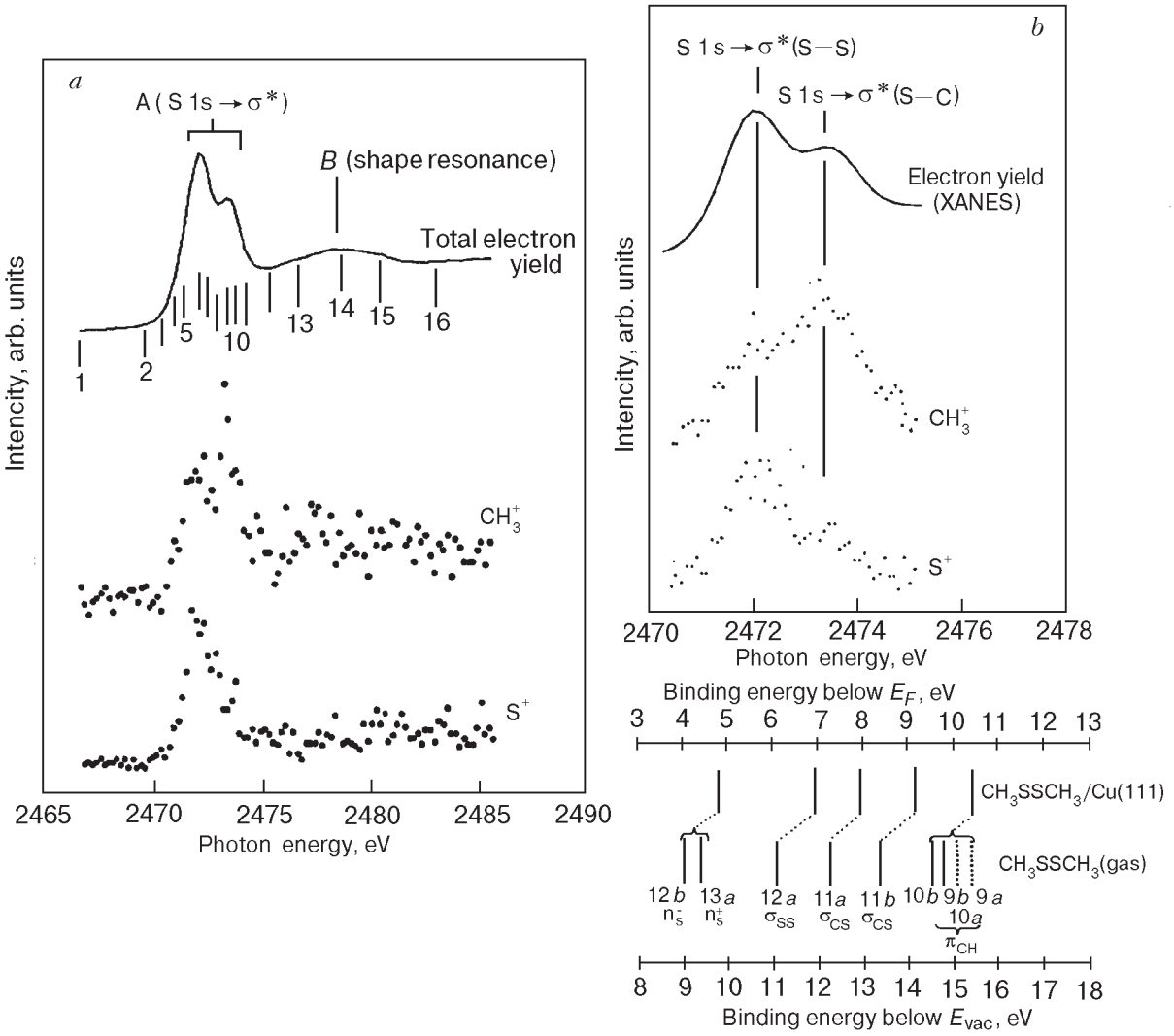

Fig. 6. Photon energy dependencies of total electron yield (solid line) and ion desorption yield (dotted lines) for multilayered dimethyldisulfide (DMDS) around the sulfur *K*-edge photoexcitation. Total electron yield curve corresponds to the x-ray absorption spectrum (XANES). The number indicated in the total electron yield curve represents the photon energy used for the measurements (Fig. 9,*a*) of Auger decay spectra (*a*). Same as Fig.6,*a* but in an expanded energy scale around the S1*s* → σ* resonance (*b*).

the S 1*s* → $\sigma^*_{(S-C)}$ excitation (Fig. 6,*b*). The latter feature clearly shows that the site-specific desorption apparently happens by the photoexcitation from the same core orbital to the different unoccupied valence orbitals. If the excited electrons are localized at the respective chemical bonds until the fragmentation happens, the observed tendency that the S 1*s* → $\sigma^*_{(S-S)}$ resonance yields S^+ desorption and S 1*s* → $\sigma^*_{(S-C)}$ resonance induces CH_3^+ desorption is quite natural because both of the σ* orbitals are strongly antibonding. The localized nature of the primary photoexcitations will be discussed on the basis of the Auger decay spectra in the next section.

6. Auger decay and mechanism of ion desorption

6.1. Patterns of Auger decay

In the previous sections, I have presented some examples where the core-level excitations induce highly element-specific and site-specific ion desorptions. The data for the element specific desorption show that the localization of the core-electrons is the main cause of the specific ion desorption. Also the results for the site-specific desorption indicate that the localization of the excited electrons in the anti-bonding state plays an important role in the specific ion desorption. Since the core-level excitation in low-*Z* elements is primarily followed by the Auger decay [49], I shall next present the Auger decay spectra in the present systems.

Let us first explain the Auger decay patterns in the present systems. For the third-row elements, the main decay channel following the ionization of the K-shell electron is primarily $KL_{2,3}L_{2,3}$ Auger transition (radiative decay, i.e., fluorescence x-ray emission plays a minor role in the present system, therefore it is not considered here).

Figure 7 shows the three types of the Auger transitions which happen around the ionization threshold. The excitation into the continuum is followed by the $KL_{2,3}L_{2,3}$ normal Auger decay (a) resulting in the two holes in the $L_{2,3}$ levels. This state is further followed by the $L_{2,3}VV$ Auger decay which results in the final electronic configuration of V^{-4}, where V denotes the valence states and the superscript indicates the number of electrons taken away. The kinetic energy of the normal Auger electron is constant. For the core-to-valence resonant excitations, two other decay channels have to be taken into account. First is the participant Auger decay (b), where the excited electron participates the Auger decay process. The excited electron itself decays into the core hole, and another electron is emitted from L shell. This process is virtually identical to the photoemission of the L-shell electron. Thus, the kinetic energy of the participant Auger electrons are the same as that of photoelectron from $L_{2,3}$ shell directly excited by the photons at the same energy. The second is the spectator Auger decay (c). In this case, the excited electron remains in the unoccupied orbital as a spectator, and another electron decays into the core hole. Then another second electron is emitted. The kinetic energy of the spectator Auger electron is close to that of the normal Auger electron. Regarding the energy of the spectator Auger electrons, we have observed the kinetic energy of the Si KLL spectator Auger electrons in SiO_2 after the Si K-edge excitation shifts linearly with the incident photon energy [50,51]. This phenomenon is observed in deep-core excitations for many adsorbed, condensed and solid systems, and the cause of the energy dispersion is ascribed to the Auger resonant Raman effect [52–58]. Therefore we can easily distinguish the spec-

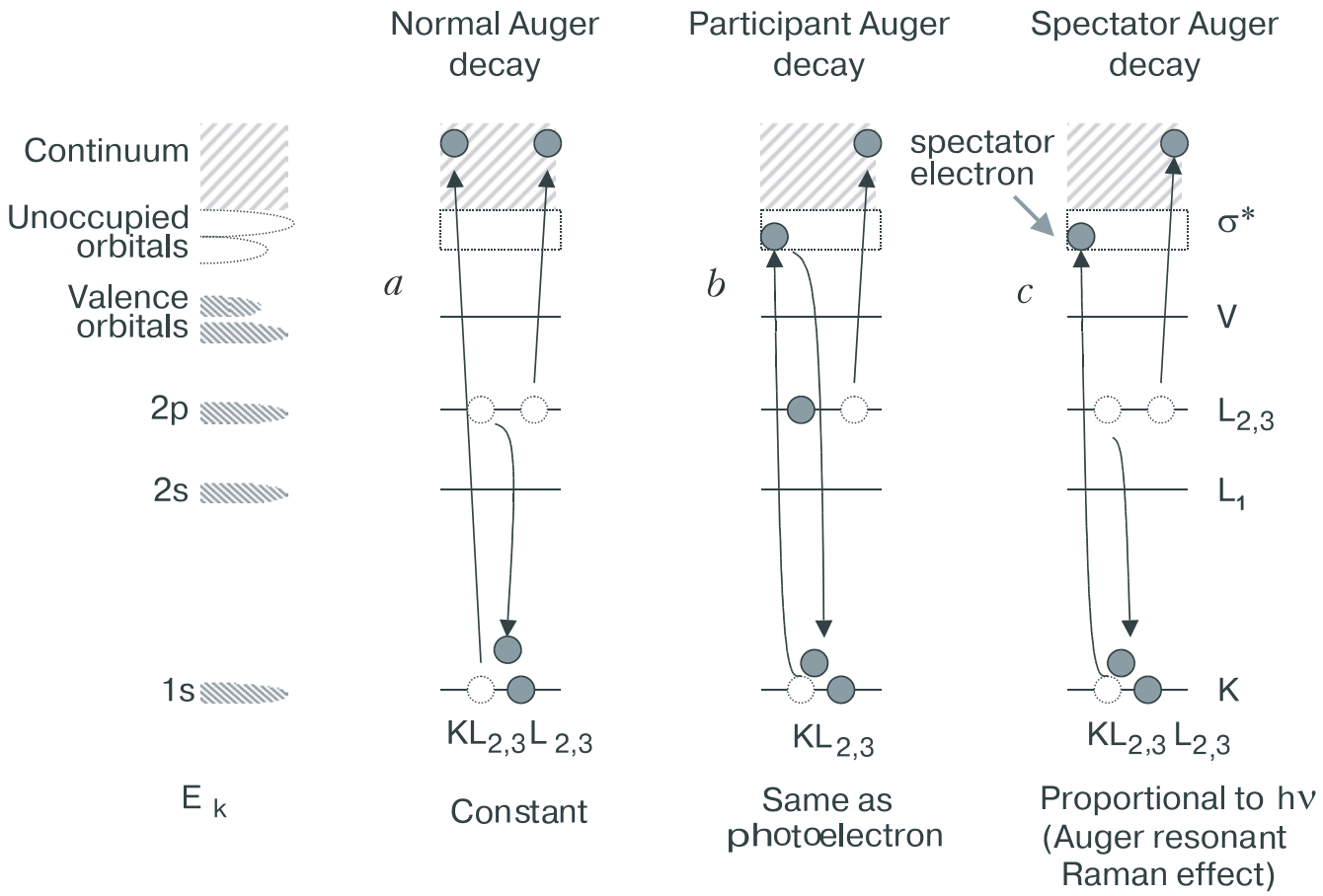

Fig. 7. Three types of the Auger transitions which happen around the inner-shell ionization threshold. The normal Auger decay following ionization is shown (a); for the core-to-valence resonant excitations, two decay channels exist; (b) is the participant Auger decay, where the excited electron participates the Auger decay; (c) is the spectator Auger decay, where the excited electron remains in the unoccupied orbital as a spectator, and another electron decays into the core hole. Then another second electron is emitted. We call the remaining electron as «spectator electron».

tator Auger peak from the normal one. The Auger resonant Raman effect more clearly shows up in condensed molecules and insulating solids than in metals and monolayered adsorbates. In the following discussion, it should be noted that the important point in the spectator Auger decay is that the excited electron remains in the unoccupied orbitals until the Auger decay. We will call the remaining electron as «spectator electron» (see Fig.7).

6.2. Condensed $SiCl_4$

Concerning the element-specific desorption, let us go back to the $SiCl_4$ case (Fig. 3). For Cl *K*-edge excitation, most of the desorbed species are Cl^+ ions. The electron and Cl^+ ion yields around the Cl *K*-edge are displayed in Fig. 8,*e* [59]. The XANES spectrum is basically in good agreement with those reported for gas-phase $SiCl_4$ [60]. Mainly three peaks are observed (numbered *2*, *4,* and *6*), which originate from Cl $1s \rightarrow \sigma^*(8a_1)$, Cl $1s \rightarrow \sigma^*(9t_2)$, and double excitation (shake-up satellite), respectively. However, a clear dissimilarity between electron-yield and Cl^+-yield curves is seen. The Cl^+ yield curve has only one maximum corresponding to the peak *2*.

The electron energy spectra taken at various photon energies are displayed in Figs. 8,*a*,*b*. Fig. 8,*a* includes the Cl *KL* participant and Cl *KLV* normal and Cl *KLV* spectator Auger decays. Fig. 8,*b* covers the Cl *KLL* normal and spectator Auger decays. In Fig. 8,*a* a slight enhancement of the Cl 2*p* photoelectron peak around the $Cl \rightarrow \sigma^*$ resonance maximum ($h\nu$ = 2823.0 eV) is observed. In the column (*c*), the intensities of the Cl 2*s* and Cl 2*p* photoelectron peaks are plotted as a function of the incident photon energy. The increase in the Cl 2*p* intensity is about 25 % at the Cl $1s \rightarrow \sigma^*(8a_1)$ resonance maximum. This enhancement corresponds to the Cl $KL_{2,3}$ participant Auger decay. In Figure 8,*b*, we can clearly see the Cl $KL_{2,3}L_{2,3}$ spectator Auger lines (peak *B*), which linearly shift to the higher energy with the increase in the photon energy. The lower kinetic-energy peaks (*A*), which are observed at high photon energies, are due to the Cl $KL_{2,3}L_{2,3}$ normal Auger electrons. The intensities of the Cl $KL_{2,3}L_{2,3}$ spectator and normal Auger peaks are plotted in the column (*d*) as a function of the photon energy. The plots of the intensity of the three types of the Auger peaks reveal that more than 98 % of the Cl $1s \rightarrow \sigma^*(8a_1)$ resonance excitation is followed by the spectator Auger decays (including *KLL* and *KLV*), while the contribution of the Cl 2*p*-derived participant decay is less than 2 %. It is also seen that the excitation at peak *6* is followed only by the normal Auger decay. The most intrinsic difference between normal and spectator Auger decays is

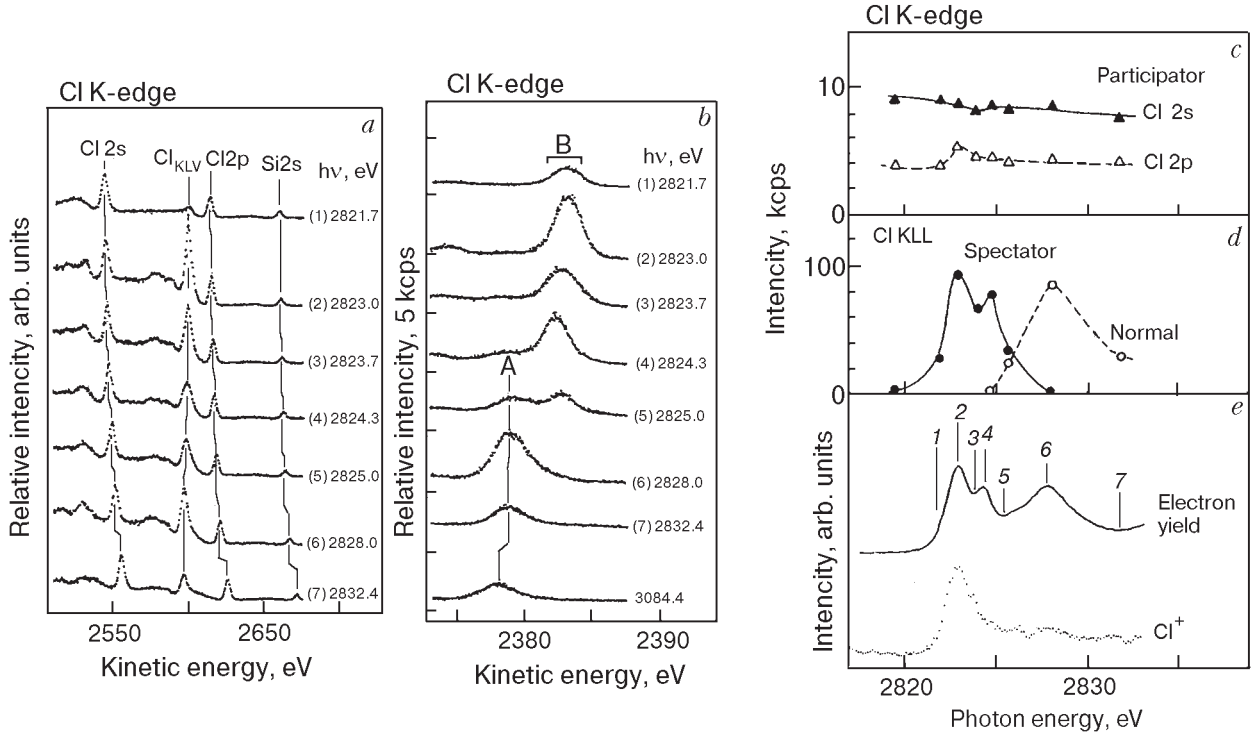

Fig. 8. Auger decay spectra of multilayered $SiCl_4$ in Cl $KL_{2,3}$ participant (*a*) and Cl $KL_{2,3}L_{2,3}$ spectator (*b*) regions excited by various photon energies around the Cl *K*-edge. In the right figures, the intensities of the resonance peaks as well as total electron yield and Cl^+ yield are plotted as a function of the photon energy.

whether or not the excited electron remains in the unoccupied orbitals in the course of the Auger electron emission (see Fig. 7). For the excitation at peak *6*, therefore, the excited electron is immediately delocalized before the movement of the Cl atom. Thus it is concluded that the existence of a «spectator electron» in the σ^* orbital is essential for the fragmentation which results in the Cl^+ desorption.

When we compare two σ^* resonances with different symmetry, i.e., $8a_1$ (peak *2*) and $9t_2$ (peak *4*), the Cl^+ ions desorb mainly at peak *2* rather than at peak *4*, although both excitations result in the spectator Auger decay. Coulman et al. have found that the desorption of H^+ ions from a multilayer of H_2O after O 1*s* excitation is extremely enhanced by the O $1s \to 4a_1$ excitation [61,62]. They have ascribed this phenomenon to the strong antibonding character of the $4a_1$ orbital. The present results for $SiCl_4$ can be interpreted in a similar manner. The contents of the Cl $3p^*$ orbital component is higher in the $8a_1$ than in the $9t_2$ [63], consequently the spectator electron in the $8a_1$ is more effective for the dissociation of the Si—Cl bond than the spectator electron in the $9t_2$. This speculation supports the above conclusion that the spectator electron in an antibonding orbital is essential for Cl^+ desorption. The high desorption yield by the Cl $1s \to \sigma^*(8a_1)$ resonance indicates that the nuclear motion of the Si—Cl bond is equivalent to or faster than the core life time. This means that the Franck-Condon transition cannot be applied to the bond dissociation process. As described above, such ultrafast non-Franck-Condon-like dissociation was reported for H^+ desorption by core excitation from condensed molecules such as H_2O [61,62] and benzene [64]. The present results reveal that such a non-Franck-Condon-like process exists even for the desorption of heavier atoms like chlorine.

6.3. Condensed $(CH_3S)_2$

Again, we go back to the site-specific desorption in condensed DMDS (Fig. 6). In this case, the most intense Auger lines after the S $1s \to \sigma^*$ excitation would be sulfur $KL_{2,3}L_{2,3}$ spectator Auger lines and sulfur $KL_{2,3}$ participant Auger line. The former appears near the sulfur $KL_{2,3}L_{2,3}$ normal Auger line and the latter is observed as the enhancement of the sulfur $L_{2,3}$(S $2p$) photoelectron. The Auger-decay spectra around the sulfur $KL_{2,3}L_{2,3}$ region taken at various photon energies around the S $1s \to \sigma^*$ resonance are shown in Fig. 9,*a*. The number indicated in each spectrum corresponds to the photon energy shown in the electron-yield curve in Fig. 6,*a*. The normal Auger peak with fixed kinetic energy apparently begins to appear from spectrum *11*. The higher kinetic-energy peaks observed in the spectra *2–11* originate from the spectator Auger decay. Linear kinetic-energy shift with the photon energy is also observed for the spectator Auger peaks. In Fig. 9,*b*, the kinetic energies of the sulfur $KL_{2,3}L_{2,3}$ Auger peaks are plotted as a function of incident photon energy. A two-step linear kinetic-energy dispersion is clearly observed in the spectator Auger peaks. Such two-step linear dispersion was explained by a fact that two kinds of the resonant excitations induce respective Auger resonant Raman effect. When the photon energy regions of linear dispersions are compared with those of the double structures in XANES spectrum (Fig. 6,*a*), the first linear line marked as spectator (*1*) corresponds to the sulfur $KL_{2,3}L_{2,3}$ spectator Auger peak following the S $1s \to \sigma^*_{(S-S)}$ excitation, and the second one marked as spectator (*2*) originates from that following the S $1s \to \sigma^*_{(S-C)}$ excitation. Therefore it is important that both the S $1s \to \sigma^*_{(S-S)}$ and S $1s \to \sigma^*_{(S-C)}$ excitations are primarily followed by the respective spectator Auger decays. This finding suggests that the spectator electrons are localized at the respective chemical bonds in the course of the Auger decay. Fig. 9,*c* summarizes the photon-energy dependencies of the peak intensities of various Auger lines. We have measured the other possible primary decay channels such as sulfur $KL_1L_{2,3}$, KL_1L_1, $KL_{2,3}V$, and KL_1V spectator decays and sulfur KL_1 participant decays, but it was turned out that the contributions of these decay channels are less than 10 % of the $KL_{2,3}L_{2,3}$ decay. When we compare Fig. 9,*c* with the XANES spectrum in Fig. 6,*a*, it is revealed that the S $1s \to \sigma^*$ resonant excitation is mostly followed by the sulfur $KL_{2,3}L_{2,3}$ spectator Auger decay but the participant decay channels play a minor role. Also it is seen that the shape resonance is virtually followed by the sulfur $KL_{2,3}L_{2,3}$ normal Auger decay.

The main decay channels and possible sequences of the electronic configurations are summarized in Table concerning the four primary excitation modes, i.e., S $1s \to \sigma^*_{(S-S)}$ resonance, S $1s \to \sigma^*_{(S-C)}$ resonance, shape resonance and S 1*s* ionization. In this table, σ^{*1} represents the spectator electron and v denotes the valence orbital. The positive and negative indices marked in the orbital show the number of electron and holes, respectively. The primary $KL_{2,3}L_{2,3}$ transitions are followed by the $L_{2,3}VV$ Auger decays where V represents the valence orbital. It was shown that the $2p^{-2}\sigma^{*1}$ state created by the $KL_{2,3}L_{2,3}$ spectator Auger decay in a similar molecule is followed by the initial $L_{2,3}VV$ Auger decay with one $2p$ hole which yields two valence holes, and succeeding $L_{2,3}VV$ decay without $2p$ hole which yields four valence holes. Although we could not distinguish between spectator and normal Auger decays in $L_{2,3}VV$ Auger decay spec-

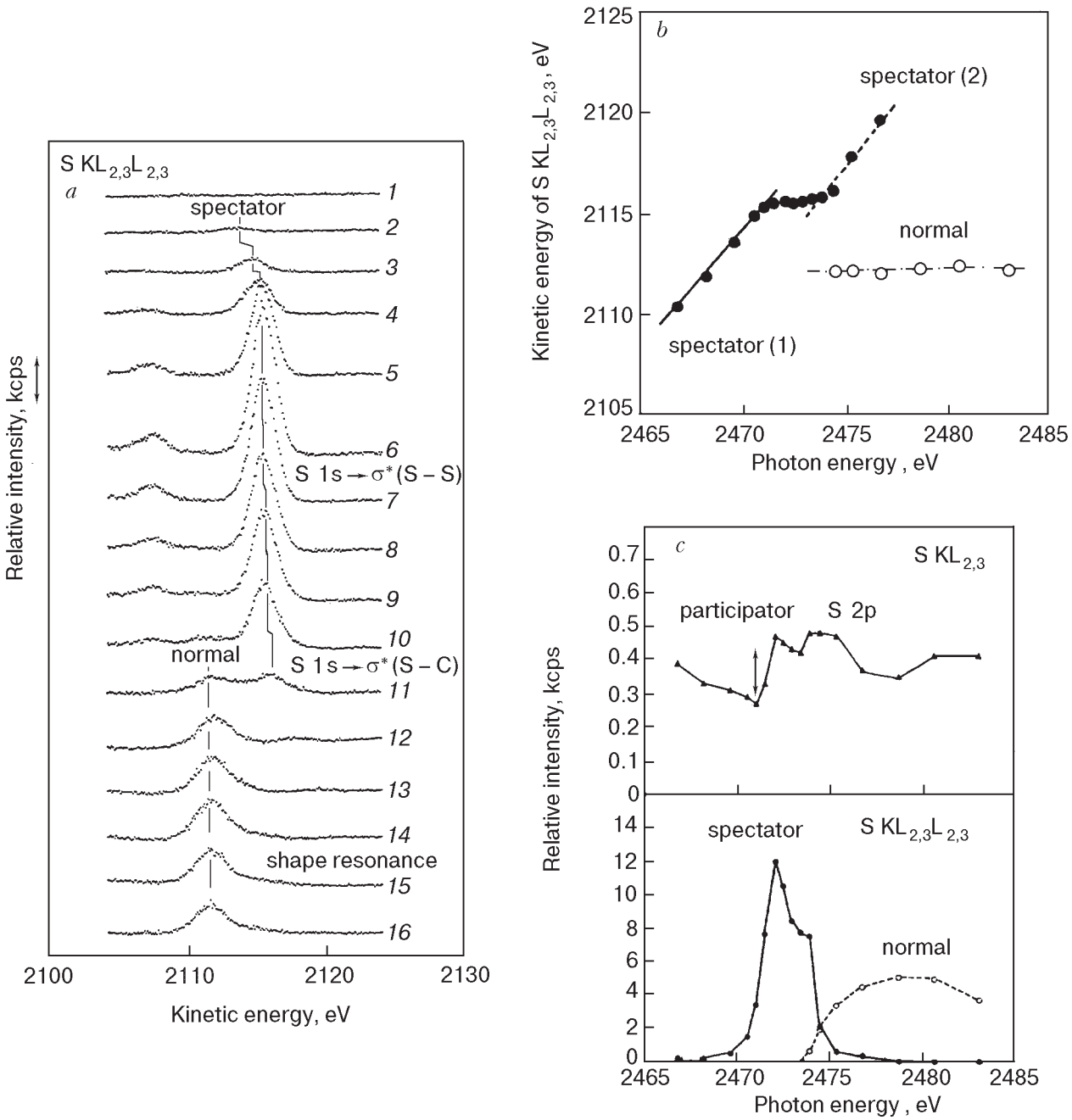

Fig. 9. Auger decay spectra of multilayered DMDS in sulfur $KL_{2,3}L_{2,3}$ region excited by various photon energies around the sulfur *K*-edge. The number indicated in each spectrum corresponds to the photon energy shown in the total electron yield curve in Fig. 6,*a* (*a*). Relation between incident photon energy and the kinetic energy of the sulfur $KL_{2,3}L_{2,3}$ Auger line for multilayered DMDS around the sulfur *K*-edge excitation (*b*). Intensities of the Auger peaks as a function of photon energy (*c*).

tra due to the broad peak structures, we tentatively assign that the spectator Auger decay would be predominant by taking the *KLL* results into consideration. Thus the final electronic configuration at the $S\,1s \rightarrow \sigma^*$ resonance is shown as $v^{-4}\sigma^{*1}$ in Table.

It has been established that the positive-ion desorption following the inner-shell ionization is in many cases well explained on the basis of the localization of two or more positive holes in valence orbitals which are created by the sequence of the Auger decays (KF-model) [65]. The Coulomb interaction between the two holes in an Auger final state leads to the localization of this state if the Coulomb energy is larger than the band width of the corresponding hole state. Then finally the fragmentation and desorption due to the Coulomb repulsion will happen. This scenario is indeed the case for the adsorbed molecules (condensate) with relatively narrow band width of one-hole state, except for monolayered

Table

The main Auger decay channels and possible sequences of the electronic configurations; v represents one of the valence orbitals, and the index shown in each orbital denotes the number of electrons; σ^{*1}_{S-S} and σ^{*1}_{S-C} are the spectator electrons localized in the S—S and S—C bonds, respectively.

Excitation mode	Electronic configuration	Desorption
S $1s \rightarrow \sigma^*_{S-S}$	$[1s^{-1}\sigma^{*1}_{S-S}] \rightarrow [2p^{-2}\sigma^{*1}_{S-S}] \rightarrow [2p^{-1}v^{-2}\sigma^{*1}_{S-S}] \rightarrow [v^{-4}\sigma^{*1}_{S-S}]$ $KL_{2,3}L_{2,3}$ (spectator) $\quad L_{2,3}VV \quad L_{2,3}VV$	$\rightarrow S^+, CH_3^+$
S $1s \rightarrow \sigma^*_{S-C}$	$[1s^{-1}\sigma^{*1}_{S-C}] \rightarrow [2p^{-2}\sigma^{*1}_{S-C}] \rightarrow [2p^{-1}v^{-2}\sigma^{*1}_{S-C}] \rightarrow [v^{-4}\sigma^{*1}_{S-C}]$ $KL_{2,3}L_{2,3}$ (spectator) $\quad L_{2,3}VV \quad L_{2,3}VV$	$\rightarrow$ mostly, CH_3^+
S $1s \rightarrow 3d^*(5s^*)$	$[1s^{-1}3d^{*1} \rightarrow [2p^{-2}] \rightarrow [2p^{-1}v^{-2}] \rightarrow [v^{-4}]$ $KL_{2,3}L_{2,3}$ (normal) $\quad L_{2,3}VV \quad L_{2,3}VV$	$\rightarrow$ few
S $1s \rightarrow$ ionization	$[1s^{-1}] \rightarrow [2p^{-2}] \rightarrow [2p^{-1}v^{-2}] \rightarrow [v^{-4}]$ $KL_{2,3}L_{2,3}$ (normal) $\quad L_{2,3}VV \quad L_{2,3}VV$	$\rightarrow$ few

adsorbates on metal substrate where the valence holes are well screened by the electrons in metal substrate (discussed in the following section). Also in the present case, the KF-process would be predominant in the photon energy range where the normal Auger decay happens. On the other hand, at the core-to-valence resonant excitation where the spectator Auger decay happens, the effect of the remaining electron in the σ* orbital on the desorption process must be also taken into account. If the KF-model can be applied not only to the core-ionization but also to the resonant core excitation, the photon-energy dependence curve of the ion desorption yield would be identical to that of the total electron yield, because the total electrons are mostly composed of inelastically scattered low-energy electrons irrespective of the primary Auger decay processes. However this is not the case for the present results (Fig. 6). Therefore, the observed dissimilarity between the XANES spectrum and ion yield curve suggests that there exist the other process than the KF- process in the S^+ and CH_3^+ desorption.

The first point of the dissimilarity is the disappearance of the shape resonance peak in the desorption-yield curves (Fig. 6,*a*). This result implies that the desorption of some fragment-ion is enhanced by a special core-to-valence photoexcitation mode. Similar results have been reported for condensed H_2O [61,62] and benzene [64] at the *K*-edge photoexcitation. Also the present authors have observed the enhancement of the atomic Cl^+ desorption from multilayered CCl_4 and $SiCl_4$ [66] at the Cl *K*-edge excitation, where the Cl $1s \rightarrow \sigma^*$ resonant excitation yields Cl^+ desorption but higher-energy resonances such as Cl $1s \rightarrow 3d^*$ and $5s^*$ do not induce scarcely any Cl^+ desorption. In both sulfur and chlorine cases, the primary decay channels at the higher-energy resonances are completely $KL_{2,3}L_{2,3}$ normal Auger decay. This fact implies that the final electronic configuration like V^{-4} does not so much contribute to the fragmentation and ion desorption. Namely the spectator electron in the σ* orbital is essential for the fragmentation.

The second point of the dissimilarity between electron and ion yield curves is the intensity ratio of the S $1s \rightarrow \sigma^*_{(S-S)}$ and S $1s \rightarrow \sigma^*_{(S-C)}$ peaks (Fig. 6,*b*). The Auger decay spectra show that both resonances are predominantly followed by the sulfur $KL_{2,3}L_{2,3}$ spectator Auger decay. As discussed above, the high desorption yield of Cl^+ ions at the Cl $1s \rightarrow \sigma^*$ resonance in adsorbed $SiCl_4$ is due to the excited electron (spectator electron) in the highly antibonding σ* orbital. Similarly, the high desorption yields of the CH_3^+ and S^+ ions at the S $1s \rightarrow \sigma^*$ resonances in comparison with those at higher-energy excitation is interpreted in terms of the spectator electrons in the highly antibonding σ* orbital. The special point in the present case is that the spectator electrons in the $\sigma^*_{(S-S)}$ and $\sigma^*_{(S-C)}$ bonds are localized at the respective sites as was confirmed by the two-step linear kinetic-energy dispersion (Fig. 9,*b*). Therefore the spectator electrons localized at the $\sigma^*_{(S-C)}$ orbital would break the S—C bond, while those localized at the $\sigma^*_{(S-S)}$ orbital would cut the S—S bond. The cleavage of the S—C bond will mainly produce the CH_3^+ ions (higher charged ions such as CH_3^{2+} were not sepa-

rated in the present experiment). On the other hand, the S—S bond breaking may produce CH_3S^+ ions. However, the intensity of the CH_3S^+ ions at the S $1s \rightarrow \sigma^*_{(S-S)}$ resonance is extremely low, and only CH_3^+ and S^+ ions are observed in comparable intensity. Concerning the desorption of molecular ions, we have observed that the desorption of the relatively light atomic Cl^+ ions from solid CCl_4 is induced by the spectator electron in the σ^* orbital, but the desorption of heavier molecular CCl_3^+ ions is not specially caused by the Cl $1s \rightarrow \sigma^*$ resonance due to the slow movement of such heavier molecular species [66]. This explanation holds for the absence of the CH_3S^+ desorption at the S $1s \rightarrow \sigma^*_{(S-S)}$ resonance. We consider that the comparable yields of the CH_3^+ and S^+ ions in mass spectrum are ascribed to the dissociation of the CH_3S^+ in the course of the desorption process.

7. Direct and indirect processes in x-ray induced ion desorption

Up to here, we have presented some examples where the core-to-valence resonance excitations in condensed and solid molecules induce element-specific and site-specific ion desorption. The remaining question is «In what case such specific reaction happen?» and the other way, «In what case specific reaction does not happen?» To answer these questions, it is important to separate two processes. First is «direct process». This is the reaction directly induced by core excitation. If this process is predominant in the fragmentation and desorption, a specific excitation of core-level electrons would be followed by the specific fragmentation and desorption. Second is «indirect process» or «secondary process». This is the reaction induced mainly by the secondary electrons such as photoelectrons, Auger electrons and inelastically scattered low-energy electrons. Even if the direct process at the core-to-valence resonance induces a specific reaction, the secondary electrons would also induce non-specific reaction. This situation is schematically illustrated in Fig. 10. In order to separate two processes in adsorbed systems, one of the approaches is the coincidence technique, in which the desorbed ions are detected in coincidence with the photoelectrons and Auger electrons. This approach was reviewed in details elsewhere by Mase et al. [67–70]. Another approach is to prepare well-controlled mono- and multilayered films of molecules on a substrate, and compare the desorption features between adsorbate-excitation and substrate-excitation. The main idea is as follows. For the multilayer, the core excitation in the molecules takes place inside of the layer. So the effect of secondary electrons on the reaction cannot be ignored. On the other hand, if we prepare precise physisorbed

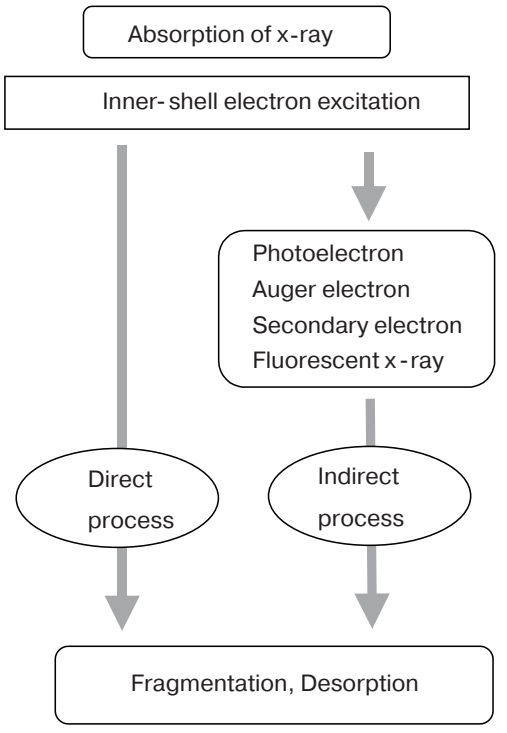

Fig. 10. Schematic of the direct and indirect processes in photofragmentation and desorption induced by inner-shell electron excitation.

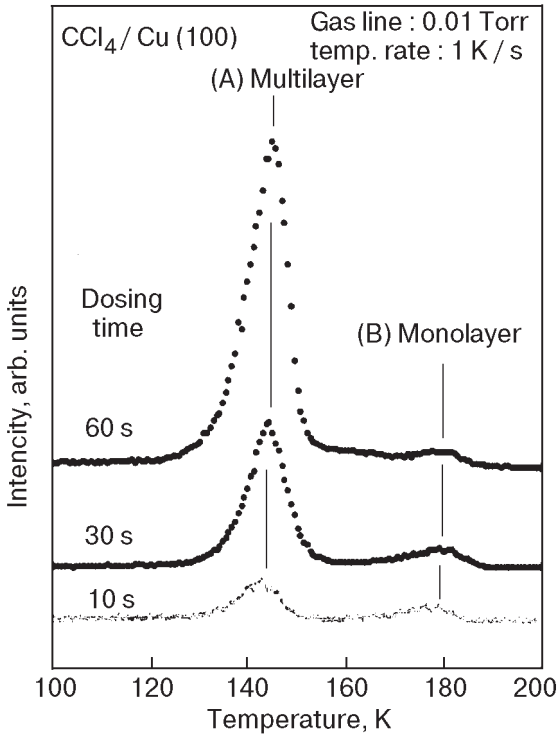

Fig. 11. Temperature-programmed-desorption spectra for CCl_4/Cu(100). The pressure of the gas-dosing vacuum line was kept at 0.01 Torr, and the surface was dosed at respective time indicated in each spectrum.

monolayer and excite only adsorbed molecules, most of the secondary electrons are emitted into vacuum, so we can pick up only direct process. For this purpose, it is essential to prepare pure physisorbed monolayer, because island structure containing multilayer region would severely affect the desorption features.

Figure 11 shows the examples of the temperature-programmed-desorption (TPD) spectra for CCl_4/Cu (100) taken at various dosing time [71]. The intensity of the lower-temperature peak (A) around 145 K proportionally increases with the dosing time, while that of the higher-temperature peak (B) around 180 K is constant. Therefore we assigned the peaks A and B as the desorption signals from physisorbed multilayer and monolayer, respectively. The number of the layer was precisely determined by the calibration curve for the intensity ratio of the peak A to peak B as a function of dosing time. For the preparation of pure monolayer, we dose several layers at 80 K, and then heat the substrate up to 165 K. This procedure results in the formation of pure homogeneous monolayer.

Figures 12,*a*,*b*,*c* show the mass spectra of the desorbed ions from CCl_4/Cu (100) at various thicknesses following the Cl $1s \rightarrow \sigma^*$ resonant photoexcitation ($h\nu = 2824.8$ eV) [72]. For multilayer, both atomic Cl^+ and molecular CCl_3^+ ions are desorbed in almost comparable intensity. In contrast, only Cl^+ ions are desorbed from monolayer. In Fig. 12,*d*, the desorption intensities of these two species are plotted as a function of the film thickness. The predominance of the Cl^+ ions compared with the CCl_3^+ ions is observed in films thinner than 3 layers. The intensities of both ions are almost saturated at 4 layers. We consider that this phenomenon is due to the difference in the mass of the desorbed species. The desorption of the Cl^+ ions is ascribed to the fast bond-breaking process due to the spectator electron in the σ^* orbital as previously discussed. This means that the movement of the Cl atom in the highly repulsive C—Cl potential curve already begins during the Auger transition overcoming the screening by the copper substrate. This may induce the CCl_3^+ desorption as a counterpart. But due to the relatively slow movement of the heavier CCl_3^+ ions, the $v^{-4}\sigma^*$ state is quenched by the screening before the desorption of the CCl_3^+ ions happens. This means that for multilayered adsorbates (molecular condensates), the screening effect on top surface layer is reduced compared with that for monolayer, because the adsorbates themselves behave a spacer layer which hinders the charge transfer screening from metal substrate. It has been reported that when a rare gas spacer layer is introduced between molecular adsorbate and metal sub-

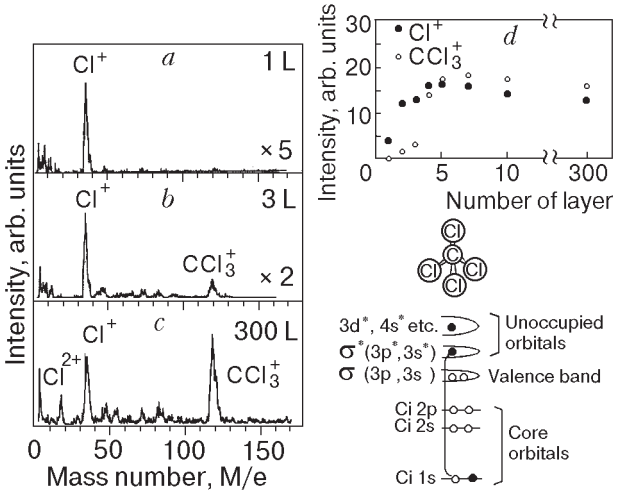

Fig. 12. Mass spectra of desorbed ions from adsorbed CCl_4 at various film thickness following the Cl $1s \rightarrow \sigma^*$ resonant photoexcitation ($h\nu = 2824.8$ eV). The number of layers indicated in each column was precisely determined by TPD measurements (*a*,*b*,*c*). Relative intensities of the Cl^+ and CCl_3^+ ions desorbed by the Cl $1s \rightarrow \sigma^*$ resonance as a function of the number of layers (*d*).

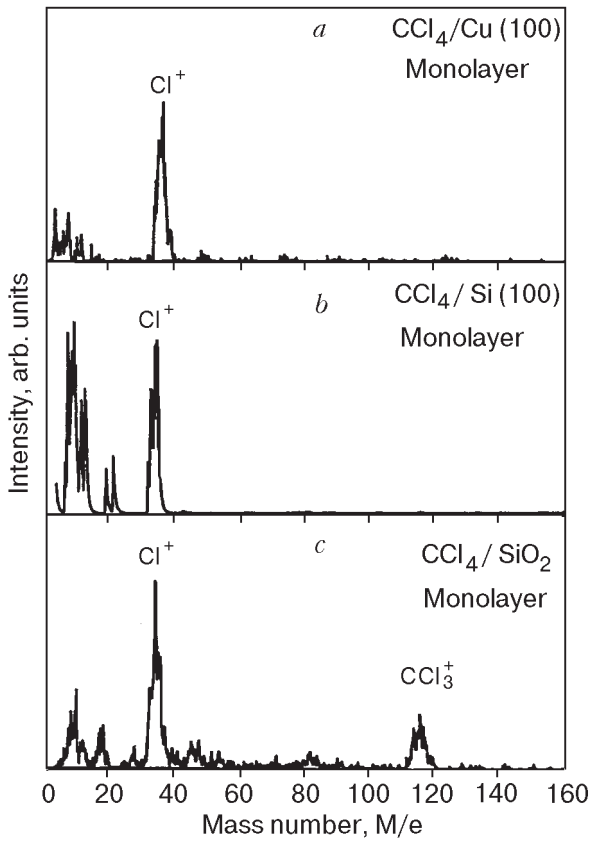

Fig. 13. Mass spectra of desorbed ions from $CCl_4/Cu(100)$ (*a*), $CCl_4/Si(100)$ (*b*), and CCl_4/SiO_2 (*c*) following the Cl *K*-edge excitation. The number of layer in each sample was precisely adjusted to be one monolayer based on the TPD measurements. The energy of the x-ray is tuned at 2824.2 eV, which corresponds to the Cl $1s \rightarrow \sigma^*$ resonance excitation.

strate, the features of electron stimulated desorption are not identical to those without spacer layer due to the weakening of the charge transfer screening [73], which is well consistent with the present results.

As to the photon-energy dependency of the desorption yield, the Cl^+ desorption from monolayer is observed only when the photon energy is tuned at the Cl $1s \rightarrow \sigma^*$ resonance in adsorbates. Note that the excitation of the substrate does not induce any ion desorption. This was clearly confirmed in similar systems where the core-to-valence resonant excitation in adsorbed thin films dominates the ion desorption over the secondary-electron-induced ion desorption following the substrate excitation [74,75].

More direct evidence for the screening effect of the substrate on the ion desorption can be obtained when we compare the ion desorption following the core excitation in physisorbed molecules by changing the electronic property of the substrate. The systems investigated are the photon-stimulated ion desorption by Cl *K*-edge excitation for monolayer of CCl_4 on metallic Cu(100) (strong coupling), semiconducting Si(100) (medium coupling), and insulating SiO_2 with wide band-gap (weak coupling) [71]. Figure 13 shows the mass spectra of the desorbed ions following the Cl *K*-edge excitation ($h\nu$ = 2824.2 eV) for monolayered CCl_4 on three different substrates. The thickness of the layers was precisely adjusted by TPD spectrum. It is clearly seen that only atomic Cl^+ ions are desorbed from monolayered CCl_4 on Cu(100) and Si(100) surfaces, while both atomic Cl^+ and molecular CCl_3^+ ions are desorbed from CCl_4/SiO_2. The difference in the mass spectral pattern suggests that excited states leading to the CCl_3^+ desorption is quenched in the strong and medium coupling systems, while they survive in weak coupling system.

Figure 14 displays the photon-energy dependencies of the total electron yields (TEY) and desorption

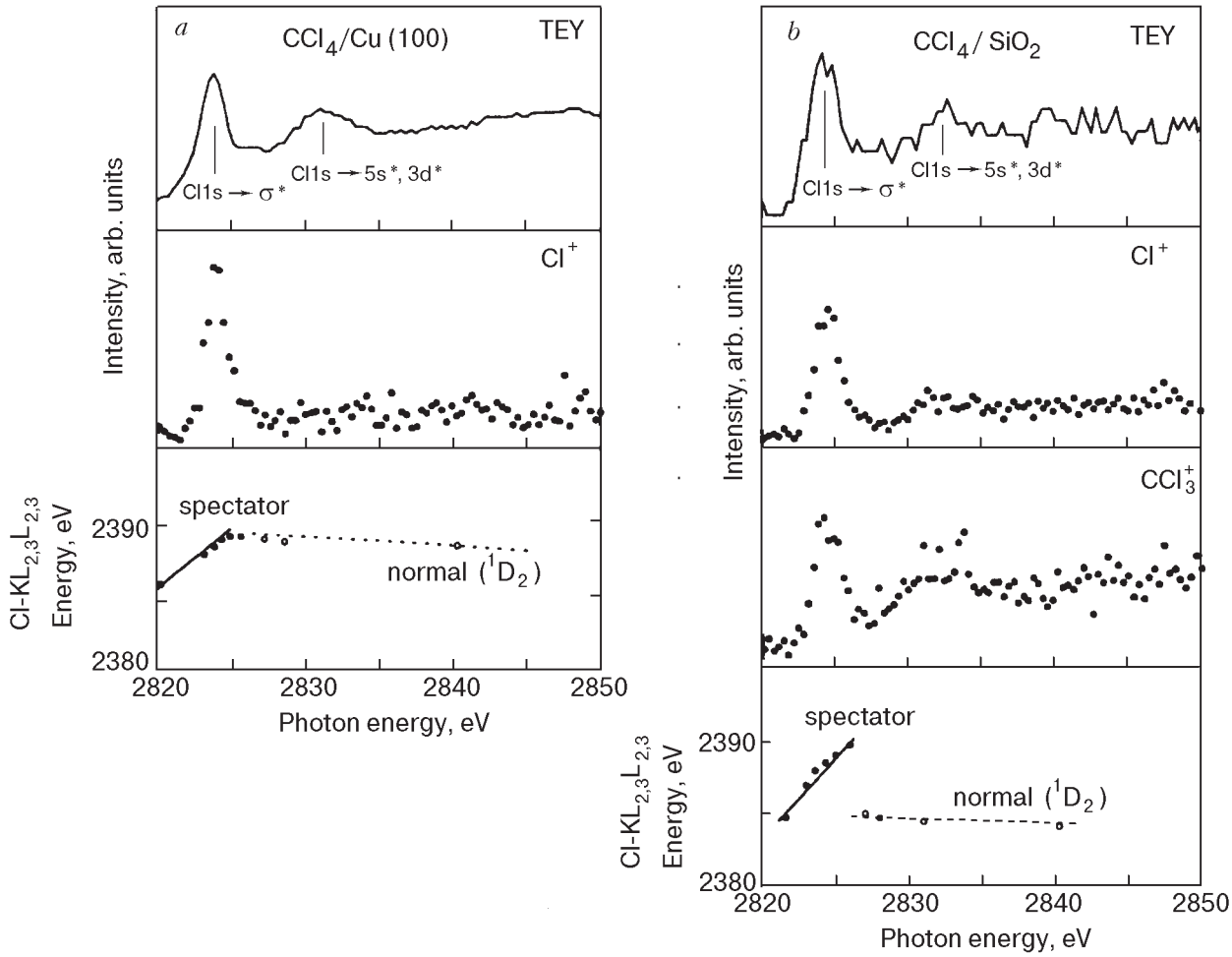

Fig. 14. Photon energy dependencies of the total electron yields (XANES) and ion desorption yields for $CCl_4/Cu(100)$ (*a*) and CCl_4/SiO_2 (*b*). In the lowest columns, the kinetic energies of the Cl $KL_{2,3}L_{2,3}$ Auger electrons are plotted as a function of the photon energy.

yields around the Cl K-edge excitation for (a) $CCl_4/Cu(100)$ and (b) CCl_4/SiO_2. The peak positions and relative intensities of the TEY curve are almost the same as those reported for gas-phase CCl_4 and condensed CCl_4. The most intense peaks around 2824.2 eV originate from the resonant excitation from the Cl 1s to unoccupied σ^* orbital, and higher-energy peaks centered around 2832 eV are attributed to the excitations to the mixture of 5s^* and 3d^* orbitals. For $CCl_4/Cu(100)$, the Cl^+ desorption happens only at the Cl $1s \rightarrow \sigma^*$ resonance. The desorption peak at the Cl $1s \rightarrow 5s^*$, $3d^*$ resonance is missing. On the other hand, for CCl_4/SiO_2, a small maximum of the Cl^+ desorption is seen at the Cl $1s \rightarrow 5s^*$, $3d^*$ resonance.

In the lowest columns of Fig. 14, the kinetic energies of the Cl $KL_{2,3}L_{2,3}$ Auger peaks are plotted as a function of the incident photon energy. The kinetic energy of the spectator Auger peaks shifts linearly with the increase in the photon energy. This phenomenon is characteristic to the spectator Auger electron, which was interpreted in terms of the Auger resonant Raman effect [52–58] as previously discussed. Note that the discontinuity of the Cl $KL_{2,3}L_{2,3}$ energy is observed around the Cl 1s threshold, $h\nu = 2826$ eV for CCl_4/SiO_2, while the spectator Auger peak continuously changes into the normal Auger peak for $CCl_4/Cu(100)$. It was elucidated that for strongly bound molecular adsorbates the Auger decay starts from a fully relaxed neutral core excited state, independently of the primary excitation (neutral or ionic). Actually the continuous energy shifts (from spectator to normal) was observed in monolayered adsorbates, but not in multilayered adsorbates [55]. The observed discontinuity in CCl_4/SiO_2 suggests that the Auger decay below the Cl 1s threshold starts from not relaxed core excited state but fully localized $1s^{-1}\sigma^*$ state, resulting in the different final electronic configuration from that of the normal Auger decay.

On the basis of the results, the possible desorption mechanisms are as follows. For $CCl_4/Cu(100)$ and $CCl_4/Si(100)$, the Cl^+ desorption happens only at the Cl $1s \rightarrow \sigma^*$ resonance by the fast bond-breaking surviving the screening effect due to the remaining electron («spectator electron») in the highly antibonding σ^* orbital. The missing of the CCl_3^+ desorption can be again interpreted by the quenching of the $V^{-4}\sigma^*$ states by the charge transfer screening due to the relatively slow movement of molecular species. For CCl_4/SiO_2 system, on the other hand, the existence of the CCl_3^+ ions indicates that even heavy molecular species survive because the screening effect is negligible. The CCl_3^+ yield curve fairly resembles the TEY curve (Fig. 14,b). Such similarity between desorption yield curve of ionic fragment and XANES spectrum is rather ordinal phenomena in condensed layer (multilayer), and this is interpreted by the effect of the inelastically scattered low-energy secondary electrons which are emitted following the Auger transition regardless of the Auger decay types. In a weak screening substrate like insulator, such relatively slow processes like secondary electron effect survive until the molecular-ion desorption even in a monolayered molecular adsorbate. It is elucidated that such slow processes play a key role in photochemical reactions on insulator surfaces. For the Cl^+ ion desorption from CCl_4/SiO_2, the contribution of the spectator-electron-induced fast bond-breaking would be included at the Cl $1s \rightarrow \sigma^*$ resonance. However, the slightly observed Cl^+ desorption at the Cl $1s \rightarrow 5s^*$, $3d^*$ resonance (Fig. 14,b) cannot be interpreted in terms of the effect of the spectator electron because this excitation is apparently followed by the normal Auger decay whose final electronic configuration is V^{-4}. This slight enhancement would be attributed to the Coulomb repulsive force among the multi valence holes as a final state of the normal Auger decay.

8. Concluding remarks

This article summarizes recent works on the ion desorption from adsorbed molecules following the irradiation of soft x-rays. The data presented here are focused on the positive fragment-ion desorption from adsorbed and condensed molecules containing third-row elements following the K-edge excitations. The element-specific and site-specific fragment-ion desorptions are clearly observed in condensed $SiCl_4$ and $Si(OCH_3)_4$. The examples for the site-specific ion desorption are also presented for adsorbed $Si(CH_3)_3F$ and condensed $(SCH_3)_2$. Such site-specific ion desorptions are characterized by the resonant photoexcitation from the same core-level into the different unoccupied orbitals. In order to clarify the mechanism of the highly specific ion desorption, we have measured the Auger decay spectra excited by the photons around the core-level ionization thresholds and the photon-energy dependencies of the electron and ion yields. As a results, it is found the localization of the excited electrons in the antibonding valence orbitals (termed as «spectator electrons») play key roles in the specific ion desorption as well as the localization of the core-levels. The excitation of core-levels in an adsorbed system is followed by the emission of various secondary electrons which may induce non-specific reaction. Therefore we separate the direct and indirect processes by preparing well-controlled mono and multilayers. It is elucidated that the resonant excitation in thin films of adsorbates induce highly specific desorption of light atomic ions. In contrast, the

specificity becomes weak in multilayers due to the effect of the secondary electrons.

Understandings of the processes for the element-specific and site-specific fragmentation and desorption from solid surfaces will shed light on the future application of x-ray-induced photochemical processes to the modification of materials surfaces.

Acknowledgements

The works reported here have been done with the excellent collaborations of Drs. T.A. Sasaki, H. Yamamoto, K. Yoshii, Y. Teraoka, T. Sekiguchi, and I. Shimoyama of Japan Atomic Energy Research Institute (JAERI). The most of the experiments presented here were performed at the BL-27A station of the Photon Factory in the High Energy Accelerator Research Organization (KEK-PF). I am deeply grateful to the support of the stuff of the KEK-PF, in particular Professor K. Kobayashi. Also Drs. H. Motohashi, H. Konish, A. Yokoya, and the stuff of JAERI are gratefully acknowledged for the technical supports for the experiments as well as fruitful discussion.

1. R.A. Rosenberg and V. Rehn, *Synchrotron Radiat. Res*. **1**, Plenum, New York (1992), p.267.
2. R.A. Rosenberg, S.P. Frigo, and J.K. Simon, *Appl. Surf. Sci.* **79/80**, 47 (1994).
3. S. Nagaoka, K. Mase, and I. Koyano, *Trends in Chem. Phys*. **6**, 1 (1997).
4. K. Tanaka, T. Sekitani, E. Ikenaga, K. Fujii, K. Mase, and N. Ueno, *J. Electron Spectrosc. Relat. Phenom*. **101-103**, 135 (1999).
5. E.P. Bertin, *Principles and Practice of X-Ray Spectrometric Analysis*, Plenum Press, New York—London (1975), p.60.
6. B.L. Henke, E.M. Gullikson, and J.C. Davis, *Atomic Data and Nuclear Data Tables* **54**, 181 (1993). The Data of the Photoionization Cross Sections are open in the Home Page of the Center for X-Ray Optics (CXRO) at the Lawrence Berkeley National Laboratory (LBNL). (http://www-cxro.lbl.gov/).
7. S.M. Seltzer, *Radiat. Res.* **136**, 147 (1993). The Data of the Mass Absorption Coefficients are open in the Home Page of the National Institute of Standards and Technology (NIST). (http://physics.nist.gov/PhysRefData/contents.html).
8. H. Konishi, A. Yokoya, H. Shiwaku, H. Motohashi, T. Makita, Y. Kishihara, S. Hashimoto, T. Harami, T.A. Sasaki, H. Maeta, H. Ohno, H. Maezawa, S. Asaoka, N. Kanaya, K. Ito, N. Usami, and K. Kobayashi, *Nucl. Instrum. Meth. Phys. Res*. **A372**, 322 (1996).
9. R.A. Rosenberg, P.J. Love, P.R. LaRoe, V. Rehn, and C.C. Parks, *Phys. Rev*. **B31**, 2634 (1985).
10. Y. Baba, K. Yoshii, and T.A. Sasaki, *Surf. Sci*. **341**, 190 (1995).
11. Y. Baba, K. Yoshii, H. Yamamoto, T.A. Sasaki, and W. Wurth, *Proc. Inter. Symp. Mater. Chem. Nucl. Environ,* Tsukuba (1996), p. 391.
12. Y. Baba, K. Yoshii, H. Yamamoto, T.A. Sasaki, and W. Wurth, *Surf. Sci*. **377-379**, 699 (1997).
13. M. Niwano, N. Miyamoto, J.K. Simons, S.P. Frigo, and R.A. Rosenberg, *Appl. Surf. Sci*. **79/80**, 403 (1994).
14. M. Niwano, J.K. Simons, S.P. Frigo, and R.A. Rosenberg, *J. Appl. Phys*. **75**, 7304 (1994).
15. K. Kinashi, M. Niwano, J. Sawahata, F. Shimoshikiryo, and N. Miyamoto, *J. Vac. Sci. Technol*. **A13**, 1879 (1995).
16. Y. Baba and T. Sekiguchi, *J. Vac. Sci. Technol*. **A18**, 334 (2000).
17. W. Eberhardt, T.K. Sham, R. Carr, S. Krummacher, M. Strongin, S.L. Weng, and D. Wesner, *Phys. Rev. Lett*. **50**, 1038 (1983).
18. S. Nagaoka, K. Mase, M. Nagasono, S. Tanaka, T. Urisu, and J. Ohshita, *J. Chem. Phys*. **107**, 10751 (1997).
19. S. Nagaoka, K. Mase, M. Nagasono, S. Tanaka, T. Urisu, J. Ohshita, and U. Nagashima, *Chem. Phys*. **249**, 15 (1999).
20. R. Romberg, N. Heckmair, S.P. Frigo, A. Ogurtsov, D. Menzel, and P. Feulner, *Phys. Rev. Lett*. **84**, 374 (2000).
21. P. Feulner, R. Romberg, S.P. Frigo, R. Weimar, M. Gsell, A. Ogurtsov, and D. Menzel, *Surf. Sci*. **451**, 41 (2000).
22. M.C.K. Tinone, K. Tanaka, J. Maruyama, N. Ueno, M. Imamura, and N. Matsubayashi, *J. Chem. Phys*. **100**, 5988 (1994).
23. M.C.K. Tinone, T. Sekitani, K. Tanaka, J. Maruyama, and N. Ueno, *Appl. Surf. Sci*. **79/80**, 89 (1994).
24. N. Ueno and K. Tanaka, *Jpn. J. Appl. Phys. Part 1*, **36**, 7605 (1997).
25. K. Fujii, T. Sekitani, K. Tanaka, S. Yamamoto, K. Okudaira, Y. Harada, and N. Ueno, *J. Electron Spectrosc. Relat. Phenom*. **88–91**, 837 (1998).
26. K. Tanaka, T. Sekitani, E. Ikenaga, K. Fujii, K. Mase, and N. Ueno, *J. Electron Spectrosc. Relat. Phenom*. **101-103**, 135 (1999).
27. K. Fujii, H. Tomimoto, K. Isshiki, M. Tooyama, T. Sekitani, and K. Tanaka, *Jpn. J. Appl. Phys. Part 1*, (*Suppl. 1*) **38,** 321 (1999).
28. D. Menzel, G. Rocker, H.P. Steinrück, D. Coulman, P.A. Heimann, W. Huber, P. Zebisch, and D.R. Lloyd, *J. Chem. Phys*. **96**, 1724 (1992).
29. H.I. Sekiguchi, T. Sekiguchi, and K. Tanaka, *Phys. Rev*. **B53**, 12655 (1996).
30. Y. Baba, K. Yoshii, and T.A. Sasaki, *J. Chem. Phys*. **105**, 1996 (1996).
31. H. Ikeura, T. Sekiguchi, and K. Tanaka, *J. Electron Spectrosc. Relat. Phenom*. **80**, 121 (1996).
32. T. Sekiguchi, H.I. Sekiguchi, K. Obi, and K. Tanaka, *J. Phys*. **IV, 7** (C2, *X-Ray Absorption Fine Structure*, Vol. 1), 505 (1997).

33. J.M. Chen, K.T. Lu, R.G. Liu, J.W. Lay, and Y.C. Liu, *J. Chem. Phys*. **106**, 9105 (1997).
34. T. Sekitani, E. Ikenaga, K. Tanaka, K. Mase, M. Nagasono, S. Tanaka, and T. Usiru, *Surf. Sci.* **390**, 107 (1997).
35. H.I. Sekiguchi and T. Sekiguchi, *Surf. Sci*. **390**, 214 (1997).
36. J.M. Chen, K.T. Lu, R.G. Liu, J.W. Lay, Y.C. Liu, and T.J. Chuang, *J. Chem. Phys*. **108**, 7849 (1998).
37. J.M. Chen, R.G. Liu, Y.J. Hsu, S.C. Yang, Y.C. Liu, Y.P. Lee, C.R. Wen, and T.J. Chuang, *J. Chem. Phys*. **109**, 8027 (1998).
38. T. Sekitani, E. Ikenaga, H. Matsuo, S. Tanaka, K. Mase, and K. Tanaka, *J. Electron Spectrosc. Relat. Phenom*. **88-91**, 831 (1998).
39. T. Sekiguchi and Y. Baba, *Surf. Sci*. **433-435**, 849 (1999).
40. H.I. Sekiguchi, T. Sekiguchi, M. Imamura, N. Matsubayashi, H. Shimada, and Y. Baba, *Surf. Sci*. **454–456**, 407 (2000).
41. S. Bodeur and J.M. Esteva, *Chem. Phys*. **100**, 415 (1985).
42. C. Dezarnaud, M. Tronc, and A.P. Hitchcock, *Chem. Phys*. **142**, 455 (1990).
43. C. Dezarnaud, M. Tronc, and A. Modelli, *Chem. Phys*. **156**, 129 (1991).
44. K. Kimura, S. Katsumata, Y. Achiba, T. Yamazaki, and S. Iwata, *Handbook of He I Photoelectron Spectra of Fundamental Organic Molecules*, Science Society Press, Tokyo (1981).
45. J.Tokue, A. Hiraya, and K. Shobatake, *Chem. Phys*. **130**, 401 (1991).
46. S. Bao, C.F. McConville, and D.P. Woodruff, *Surf. Sci*. **187**, 133 (1987).
47. A.P. Hitchcock, S. Bodeur, and M. Tronc, *Physica* **B158**, 257 (1989).
48. Y. Baba, K. Yoshii, and T.A. Sasaki (unpublished results).
49. M.O. Kraus, *J. Phys. Chem. Ref. Data* **8**, 307 (1979).
50. Y. Baba, T.A. Sasaki, and H. Yamamoto, *Phys. Rev*. **B49**, 709 (1994).
51. Y. Baba, H. Yamamoto, and T.A. Sasaki, *Surf. Sci*. **307**, 896 (1994).
52. T.A. Sasaki, Y. Baba, K. Yoshii, H. Yamamoto, and T. Nakatani, *Phys. Rev*. **B50**, 15519 (1994).
53. T.A. Sasaki, Y. Baba, K. Yoshii, and H. Yamamoto, *J. Phys.: Condens. Matter* **7**, 463 (1995).
54. T.A. Sasaki, Y. Baba, K. Yoshii, and H. Yamamoto, *J. Electron Spectrosc. Relat. Phenom*. **76**, 411 (1995).
55. K. Yoshii, Y. Baba, and T.A. Sasaki, *J. Electron Spectrosc. Relat. Phenom*. **79**, 215 (1996).
56. K. Yoshii, Y. Baba, and T.A. Sasaki, *J. Phys.: Condens. Matter* **9**, 2839 (1997).
57. K. Yoshii, Y. Baba, and T.A. Sasaki, *Phys. Status. Solid*. **B206**, 811 (1998).
58. K. Yoshii, Y. Baba, and T.A. Sasaki, *J. Electron Spectrosc. Relat. Phenom*. **93**, 105 (1998).
59. Y. Baba, K. Yoshii, and T.A. Sasaki, *Surf. Sci*. **357–358**, 302 (1996).
60. S. Bodeur, I. Nenner, and P. Millie, *Phys. Rev*. **A34**, 2986 (1986).
61. D. Coulman, A. Puschmann, W. Wurth, H.P. Steinrück, and D. Menzel, *Chem. Phys. Lett*. **148**, 371 (1988).
62. D. Coulman, A. Puschmann, U. Hofer, H.P. Steinrück, W. Wurth, P. Feulner, and D. Menzel, *J. Chem. Phys*. **93**, 58 (1990).
63. H. Ishikawa, K. Fujima, J. Adachi, E. Miyauchi, and T. Fujii, *J. Chem. Phys*. **94**, 6740 (1991).
64. D. Menzel, G. Rocker, H.P. Steinrück, D. Coulman, P.A. Heimann, W. Huber, P. Zebisch, and D.R. Loyd, *J. Chem. Phys*. **96**, 1724 (1992).
65. M.L. Knotek and P.J. Feibelman, *Phys. Rev. Lett*. **40**, 964 (1978).
66. Y. Baba, K. Yoshii, and T.A. Sasaki, *Surf. Sci*. **376**, 330 (1997).
67. K. Mase, M. Nagasono, S. Tanaka, M. Kamada, T. Urisu, and Y. Murata, *Rev. Sci. Instrum*. **68**, 1703 (1997).
68. K. Mase, M. Nagasono, S. Tanaka, T. Urisu, E. Ikenaga, T. Sekitani, and K. Tanaka, *J. Chem. Phys*. **108**, 6550 (1998).
69. K. Mase and S. Tanaka, *Jpn. J. Appl. Phys. Part 1*, **38**, 233 (1999).
70. K. Mase, S. Tanaka, M. Nagasono, and T. Urisu, *Surf. Sci*. **451**, 143 (2000).
71. Y. Baba and T. Sekiguchi, *Surf. Sci*. **433–435**, 843 (1999).
72. Y. Baba, K. Yoshii, and T.A. Sasaki, *Surf. Sci*. **402–404**, 115 (1998).
73. M. Scheuer and D. Menzel, *Surf. Sci*. **390**, 23 (1997).
74. J.M. Chen, S.C. Yang, and Y.C. Liu, *Surf. Sci*. **391**, 278 (1997).
75. T. Sekiguchi, Y. Baba, Y. Li, and M. Ali (unpublished results).